Electronic Supplementary Information

Surface-Enhanced Raman Imaging of Cell Membrane by Highly

Homogeneous and Isotropic Silver Nanostructure

Gianluigi Zito,* Giulia Rusciano, Giuseppe Pesce, Alden Dochshanov and Antonio Sasso

Dept. of Physics, Università degli Studi di Napoli Federico II, via Cintia 80126, Napoli, Italy

*Corresponding author: zito@fisica.unina.it

Additional Information for Ag-BCP Synthesis and Deposition

For coverslip pre-treatment, commercial standard microscope coverslips were soaked into ultrasonic bath (UB) for 22 min at 60°C in acetone and then in milli-Q water solution with sonic bath soap (3% w/w), then rinsed first with milli-Q water in UB, and then again with isopropanol (same procedure). Finally they were dried with nitrogen pump.

Structure Factor Map and Hyperuniform long range-correlations

Figure S1 shows the radial average of the structure factor map (map also depicted in **Figure 1e** of the main manuscript) of the nanostructure shown in **Figure 1c.** The structure factor is defined, for a finite point pattern configuration of N centroids, as

$$S(\mathbf{q}) = \frac{1}{N}\left|\sum_{j=1}^{N}\exp(i\mathbf{q}\cdot\mathbf{r}_j)\right|^2 \qquad (\mathbf{q} \neq 0)$$

where $\mathbf{q}$ is the wave vector and $\mathbf{r}_j$ represents the spatial coordinates of the j-th center of mass in the pattern. The forward scattering ($\mathbf{q} = 0$) is omitted for consistency with the definition of the ensemble-average structure factor of an infinite point configuration $S(\mathbf{q}) = 1 + \rho\tilde{h}(\mathbf{q})$ in which ρ is the number density, $\tilde{h}(\mathbf{q})$ is the Fourier transform of the total correlation function $h(\mathbf{r}) = g_2(\mathbf{r}) - 1$ and $g_2(\mathbf{r}) = g_2(r)$ defines the pair-correlation function of the pattern. For homogeneous and isotropic systems we can write $r = |\mathbf{r}|$. For an infinite point pattern, the structure is *hyperuniform* and shows long-range correlations when $\lim_{\mathbf{q}\to 0} S(\mathbf{q}) = 0$. In fact, such condition means that the infinite-wavelength density fluctuations ($S(0)$) are completely suppressed and hence the local number variance $\sigma^2(R)$ scales slower than R^d for large-R (d = Euclidean

space dimension, R = radius of the spherical observation window). A better description can be found in ref. [S1] (see also references therein). The degree to which long-range density fluctuations vanish can be used to rank ideal ordered crystals, quasicrystals and also disordered point patterns. Hyperuniform disordered point patterns are equivalent to ordered structures in terms of suppression of long-range density fluctuations but have the statistical properties of a glass with no Bragg peaks. The fit $S(Q) = a_0 + a_1 Q$ (with normalized $Q = qD/2\pi$) of the small-q behavior of the structure factor of our disordered nanostructure gave $a_0 = (6 \pm 4) \times 10^{-4}$ and $a_1 = 0.110 \pm 0.003$ which pointed out a nearly hyperuniform long-range behavior, namely a structure homogenous as much as a periodic one but with the advantage of isotropy introduced by disorder.
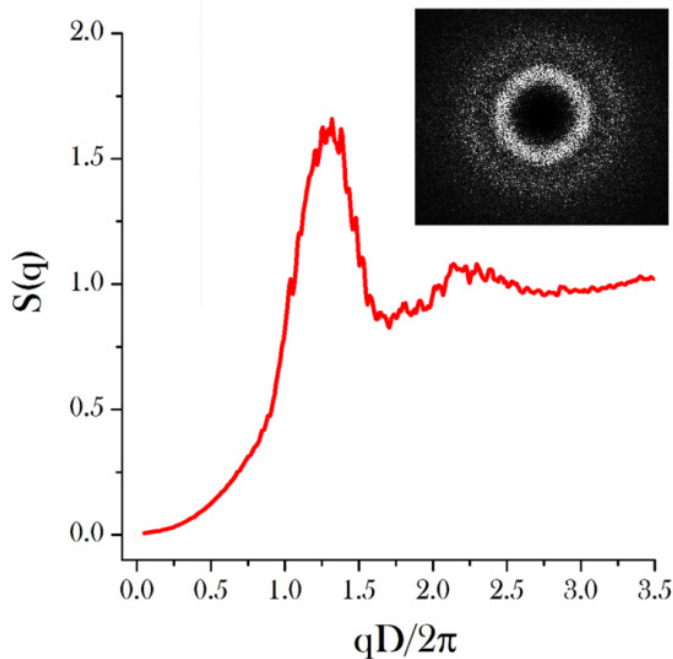

Figure S1. Structure factor $S(|q|)$ as a function of the normalized spatial frequency $qD/2\pi$, with D = 26 nm (average diameter of the micelle core). $S(|q|)$ is obtained from the radial average of the structure factor map shown in the inset. The structure factor map is obtained as above described from the disordered pattern of **Figure 1c**, in particular from digital analysis by means of a custom-made algorithm of several large scale AFM images of highly monodispersed unloaded micelles monolayers (spin coated on silicon) and SEM images of Ag-loaded micelles (on ITO-coated glass coverslips).

Additional Information on Preliminary SERS Characterization and CV Deposition

Crystal violet was diluted into a milli-Q water solution to several concentrations, namely 0.3, 3.1, 34.6, 43.8, 150, 380, 4,200, 54,000 nM. Then, the particular solution employed was infiltrated into a cell constituted by two parallel substrates (24×24 mm^2) distanced by silica beads spacers of variable diameter depending on the desired thickness of the cell, from 4.8 μm ($\pm$ 4%) to 15.0 μm ($\pm$ 4%). For larger thicknesses, PET spacers were employed. The planar cell was previously sealed at two of the external borders with UV glue. In that way the liquid was infiltrated into a precisely controlled volume. A scheme is shown in **Figure S2-A**. The entrance and flow windows retained the liquid to leak out by the surface tension of water and eventually the water evaporated towards the center of the cell. No inhomogeneity effect (coffee-ring-stain) was visible at an optical microscopy inspection when high concentrated solutions were infiltrated ($\approx$ 5 mM). In other words, the evaporation left a nearly perfect uniform layer of molecules. Molecular diffusion happened at the borders of the evaporating water surface, which was represented by the water meniscus along vertical sections of the planar cell in **Figure S2-A**. The water meniscus then moved towards the center of
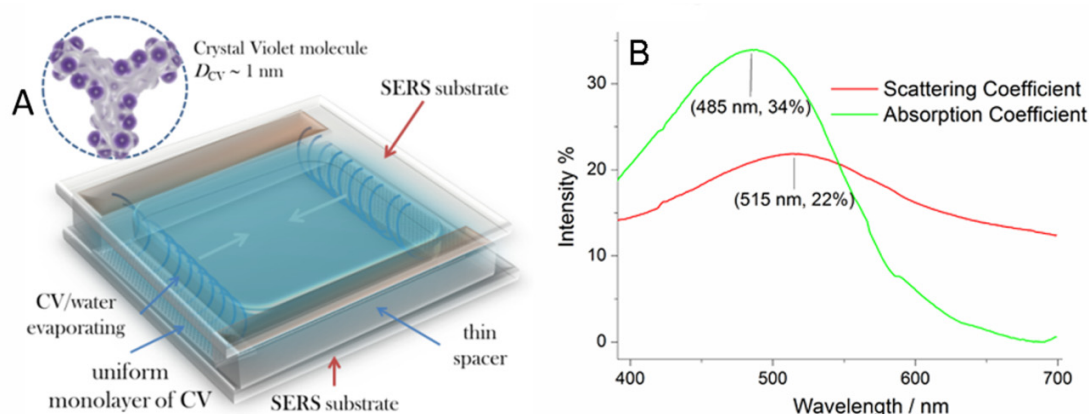

Figure S2. (A) Sketch of the uniform deposition of probe molecules based on water evaporation. (B) UV-Vis Absorption and Scattering Coefficients of the random silver nanostructure after removal of polymer by UV treatment.

the cell as the liquid evaporated and left adsorbed molecules on the top and bottom surfaces. The lateral surface of the parallelepiped was negligible because of the small thickness ($\sim$ 10 - 200 μm) of the cell with respect to the width ($\approx$ 24 mm). Being top and bottom substrates identical, an equal deposition of the molecules was envisaged on the two surfaces. Hence, the spatial density of molecules on each substrate could be straightforwardly estimated. The uniformity of the molecular distribution was verified *a posteriori* by uniformity of the spatial distribution of SERS enhancement factor as actually experimentally found for lower concentrated solution. In a second phase, an even more straightforward method of deposition was developed relying on the water surface tension properties that gave the same results. Spacers and border sealing were avoided simply by exploiting the surface tension of the water sustaining the top substrate of the cell. In other words, a 100-μl volume was left in the center and covered gently by the other glass that spread uniformly the liquid till the glass borders. The thickness of the volume embedded within the two silver-coated coverslips changed along water evaporation, always keeping a constant area of adsorption for the molecules evermore in Brownian motion.

Figure S2-B shows the UV-Vis extinction coefficient of the blank SERS substrate with close-packed random nanostructure, after polymer removal.

For evaluating the substrate enhancement factor G [S2], the Raman reference signal I_R of CV was normalized, in first place, to the number N_{vol} of the CV powder following the procedure described in ref. [S3] (by measuring the average scattering from the bulk CV powder). This led to a value of G overestimated at least of 2 orders of magnitude. Due to the strong absorption of CV molecules at 532 nm [S4] having a molar extinction coefficient approximately of $0.5 \ 10^5$ cm^{-1} M^{-1}, only the molecules from a volume with an effective thickness (penetration length) of ~ 30 nm could actually contribute to the Raman signal detected, that is just a fraction of 1% of our scattering volume. This was verified by measurements carried out in diluted water solution of CV of 1.1 mM and 5.3 mM, namely from a number of molecules orders of magnitude smaller than what contained in an equivalent volume of powder but still producing a Raman intensity comparable with the powder. For 1.1 mM and 5.3 mM, the penetration length was estimated to be, respectively, of 86 μm and 17 μm, both values much larger than our confocal thickness. This second normalization led to a sounder, reliable ratio I_R / N_{vol}. Furthermore, the reference was acquired also for a solid layer, 30-nm thick, obtained by CV deposition from a solution with concentration 100 μM and again produced the same intensity of the bulk CV powder. Estimation of the penetration lengths were carried out by integrating the Lambert-Beer law as a function of the molar concentration of the solution.

Other precautions were necessary because of the dependence of reference signal I_R on the incident power, and in minor part also on the integration time. In fact, we have experimentally found the detected signal I_R to vary linearly with power and integration time only for power incident on the CV solution < 200 μW, and for fixed power, for integration time below a few seconds. Measurements must be carried out near the boundary of the cell to avoid artifacts due to absorption. In **Figure S3**, the Raman intensity of the 1620 cm^{-1} band from a CV solution of 1.1 mM in water is shown as a function of excitation power (at 532 nm) and integration time. Above the threshold of 200 μW, I_R decreases significantly for increasing power till reaching a sort of saturation regime for power > 1.5 mW.

The experimental values used for enhancement factor estimation, as reported in the Methods section, were then I_S = 256 counts measured with an incident power P_{in} = 3.7 μW and integration time Δt = 1s, from N_{surf} = 8,683. The reference was instead I_R = 216 counts with P_{in} = 69 μW and integration time Δt = 10s and from an estimated number of molecules N_{vol} = 4.07 ×10^7, that is only a fraction of ~ 1% of the number of molecules contained within the same scattering volume for bulk powder. This value was in good agreement with what we found independently by using the Raman reference intensity measured from both 1.1-mM and 5.3-mM solutions of CV. The signals in this case were normalized to the number of molecules present in the scattering volume V_{scat} = 2.0 μm^3 estimated from the known concentration.
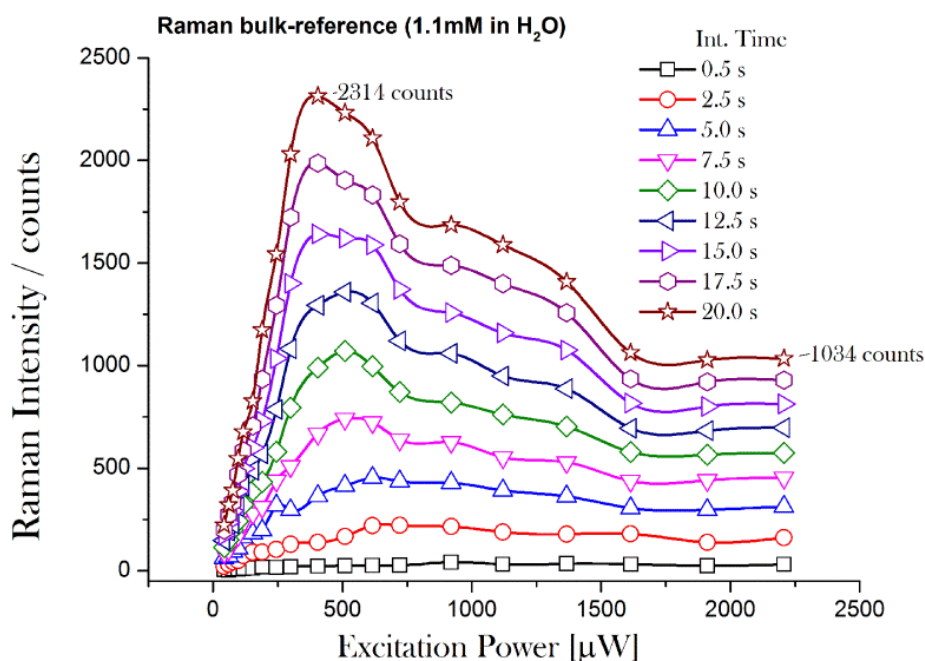

Figure S3. Bulk-Reference Raman intensity from a 1.1-mM water solution of crystal violet as a function of the incident power and by varying the integration time.

Oxidation, Substrate Stability and Nanotoxicity Issues

Our glass-supported Ag-BCP substrates were used as freshly prepared following UV irradiation and then stored in nitrogen atmosphere. In agreement with what reported for the silicon-supported Ag-BCP substrate [S3] no oxidation was found as alteration of the SERS signal [S5] after 24 h of exposure at ambient condition with incident power below 50 μW: a time much larger than what required for a SERS hyperspectral imaging. Also, we did not observe any significant detectable change of the UV-Vis spectrum along 14 days of observation. Upon exposure of the sandwiched cell substrate at ambient conditions for 60 days, we only found a reduction of the CV SERS signal of a factor ~ 2, likely ascribable to silver oxide formation. On the contrary, colloidal suspensions prepared via Lee and Meisel protocol [S6] with KCl activation [S2] did manifest oxidation and SERS instability issues.

The BCP constituents were detected in the SERS measurements of the blank substrate before UV treatment. Polymer SERS spectrum was characterized by well-defined spectral markers that matched the spontaneous Raman peaks of the bulk PS-P4VP (with different relative intensity though). However, this spectrum was sensitive to the incident power. We studied the evolution of the polymer peaks as a function of the incident power by fast time series acquisition. At an incident power of 400 µW, the polymer peaks decreased and disappeared after 2 min, leaving only a carbonaceous signature in the spectrum, probably because of heat damage. At low power, polymer spectrum remained stable for longer. After UV treatment, the polymer spectrum background consisted of only one band at ca. 660 cm^{-1} that we ascribed to P4VP - probably residues of the micelles' core in the gap between nanoparticles – or PS-P4VP fragments. It was detectable only at much higher incident power than that used in the SERS measurements on CV, R6G and RBCs. It was, in fact, 3 to 5 orders of magnitude less intense than CV or RBC scattering. Typically, the SERS blank spectrum after UV treatment was characterized by a broad luminescence spectrum of low intensity (few photon counts above the dark count), with carbonaceous signature in the range 1300 - 1600 cm^{-1}, visible increasing the incident power.

During the experiments with our Ag-BCP-based substrates, no RBC ghost formation was observed, probably because of the immobilization of the nanoparticles that prevented NPs uptake and membrane ruptures on short-term exposure of the cells. It is worth mentioning that prior the procedure of centrifugation and filtering of the Ag-BCP micelle solution, a ghost formation was indeed observable even for short-term exposure (1 h), which we ascribed to the presence of non-immobilized silver nanoparticles. For this reason, the substrates were rinsed accurately before experiments. Ghost formation was always observed when using citrate-reduced colloidal substrates [S6]. An improved immobilization of the nanostructure was observed for the disordered nanostructure of **Figure 1c** when soaked in the RBC's buffer solution for 7 days, probably because of the denser packing.

Basis Analysis

A general spectrum $\mathbf{S}(x, y)$ which consists of N different material-spectra can be expressed as a linear superposition of its elemental constituents $\mathbf{B}_k$ imposed as basis functions according to $\mathbf{S}(x, y) = \sum_{k=1}^{N} \alpha_k(x, y)\mathbf{B}_k$. It is possible to estimate the weighting factors (or projecting coefficients) $\alpha_k(x, y)$ by a least squares fit. The weighting factors are proportional to the scattering intensities of the elemental constituents within the scattering area. A quantitative analysis requires their different scattering efficiencies to be taken into account. The algorithm fits each spectrum of a multi-graph ensemble with a linear combination of the basis spectra using the least squares method.

Additional Information on inter-cluster coupling by Finite Element Method Simulations

In **Figure S4**, the spatial distributions of the (approximated) enhancement factor $G = |E_s/E_i|^4$ (log-scale) in the section plane $z = 0$ for single (a) and double cluster (b) are shown, respectively. The enhancement strength is saturated to improve the comparison. The area of saturated enhancement is increased in (b) because of the near-field interaction established between the NPs in the two clusters. However, in our simulations such an *inter-cluster* coupling produces a relatively small variation on the spatial average of the enhancement factor of the

structure (normalized to the unitary volume of each cluster) $G_{av} = \langle G \rangle$ if compared to the *intra-cluster* contribution. So, in our nanostructure, *inter-cluster* coupling induced an increase of the volume fraction of fixed enhancement, but did not alter significantly the resulting average

$G_{av} = \langle G \rangle$ as contributing only a factor of the order of ~ 1 - 3, in agreement also with experimental results reported by Yan *et al.* about periodic arrays of clusters of nanoparticles in strong coupling regime [S7]. Also when considering a dimer of clusters (minimum gap ~ 3 nm) with slightly different morphologies, namely a slightly varied random configuration of the nanoparticles, the more important consequence seems the increase of the volume fraction of defined level of enhancement as in the case of equal clusters of **Figure S4**.

In addition, from our simulations, the distance-range of the enhancement is barely affected by inter-cluster coupling as G_{av} rapidly vanishes, like in the case of single-cluster, at a distance larger than the radius of the outer shell of the cluster.
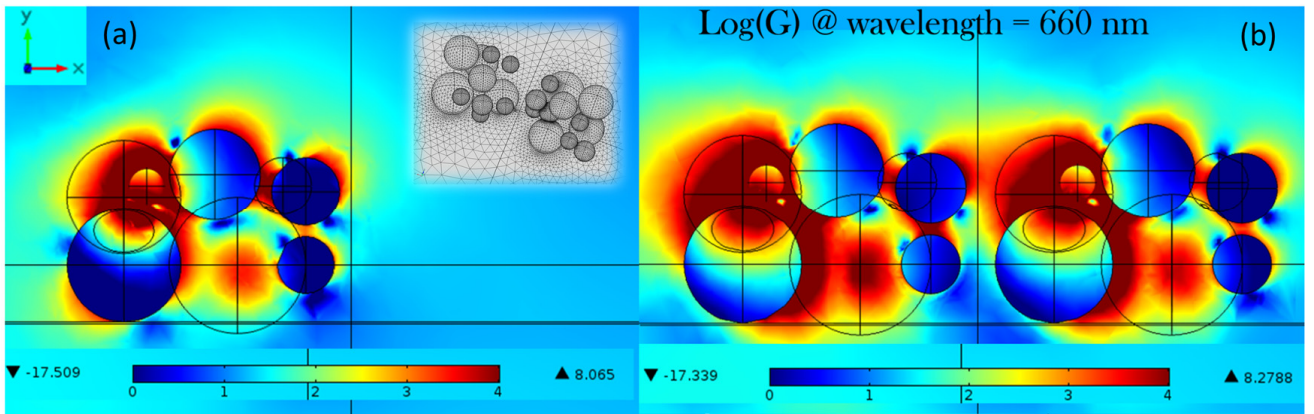

Figure S4. Spatial distributions of the enhancement factor $G(x, y)$ in the section plane $z = 0$ for single (a) and double cluster (b), calculated on glass substrate and in water environment: a saturation on the colormap (log-scale) was imposed at 10^4. The inset in (a) shows the surface mesh in the modelled geometry. Total diameter of the single cluster: $D \sim 26$ nm.

Raman Assignment

Conventional Raman Scattering Spectra (CR) of live-RBC and RBC Ghosts

Figure S5 shows the typical spontaneous conventional Raman (CR) spectrum of a viable RBC immobilized on glass coverslip (by spontaneous electrostatic interaction). The RBC was stable in shape and position for at least 8 hours. As can be seen from **Figure S4**, the high resolution CR spectrum of the live RBC mainly reflects only the haemoglobin (Hb) contented in the cell volume, in any position of the cell. Well-known observed Raman bands, in this case, belong to the porphyrin chromophore of Hb, in agreement with refs [S8, S9].
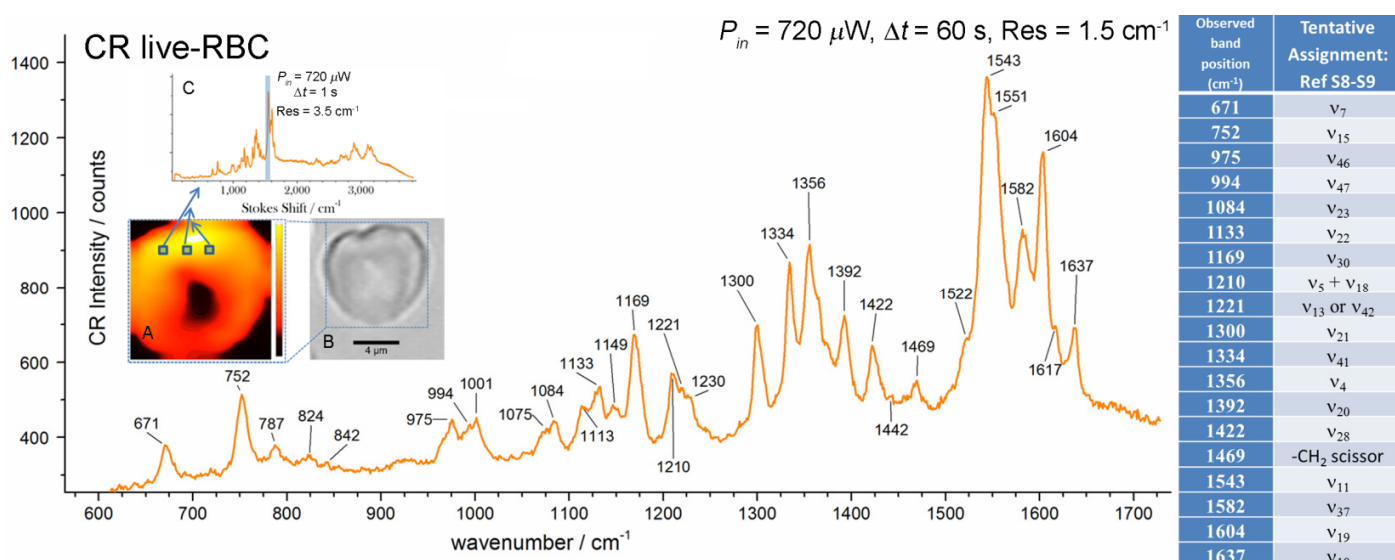

Observed band position (cm^{-1})	Tentative Assignment: Ref S8-S9
671	ν_7
752	ν_{15}
975	ν_{46}
994	ν_{47}
1084	ν_{23}
1133	ν_{22}
1169	ν_{30}
1210	$\nu_5 + \nu_{18}$
1221	ν_{13} or ν_{42}
1300	ν_{21}
1334	ν_{41}
1356	ν_4
1392	ν_{20}
1422	ν_{28}
1469	-CH$_2$ scissor
1543	ν_{11}
1582	ν_{37}
1604	ν_{19}
1637	ν_{10}

Figure S5. Spontaneous Conventional Raman (CR) of live RBC, mainly reflecting hemoglobin (Hb) content. In the Table on the right, the main Raman assignment. In the inset, Raman imaging (A) obtained from the RBC shown in (B) (optical image) by projecting the integrated intensity of the main spectral features (1500 - 1600 cm^{-1}) (C) produced by the Hb molecules: the spectra acquired in different positions are ascribable always to hemoglobin as shown in (C) but the intensity map (A) reflects the morphology of the cell because the intensity of the signal is modulated according to the density of molecules intersected in the scattering volume. The raster scan was conducted at the equatorial plane 1.5 μm above the bottom coverslip, with lower integration time ($\Delta t \sim 1$s) to preserve the cell during scansion.
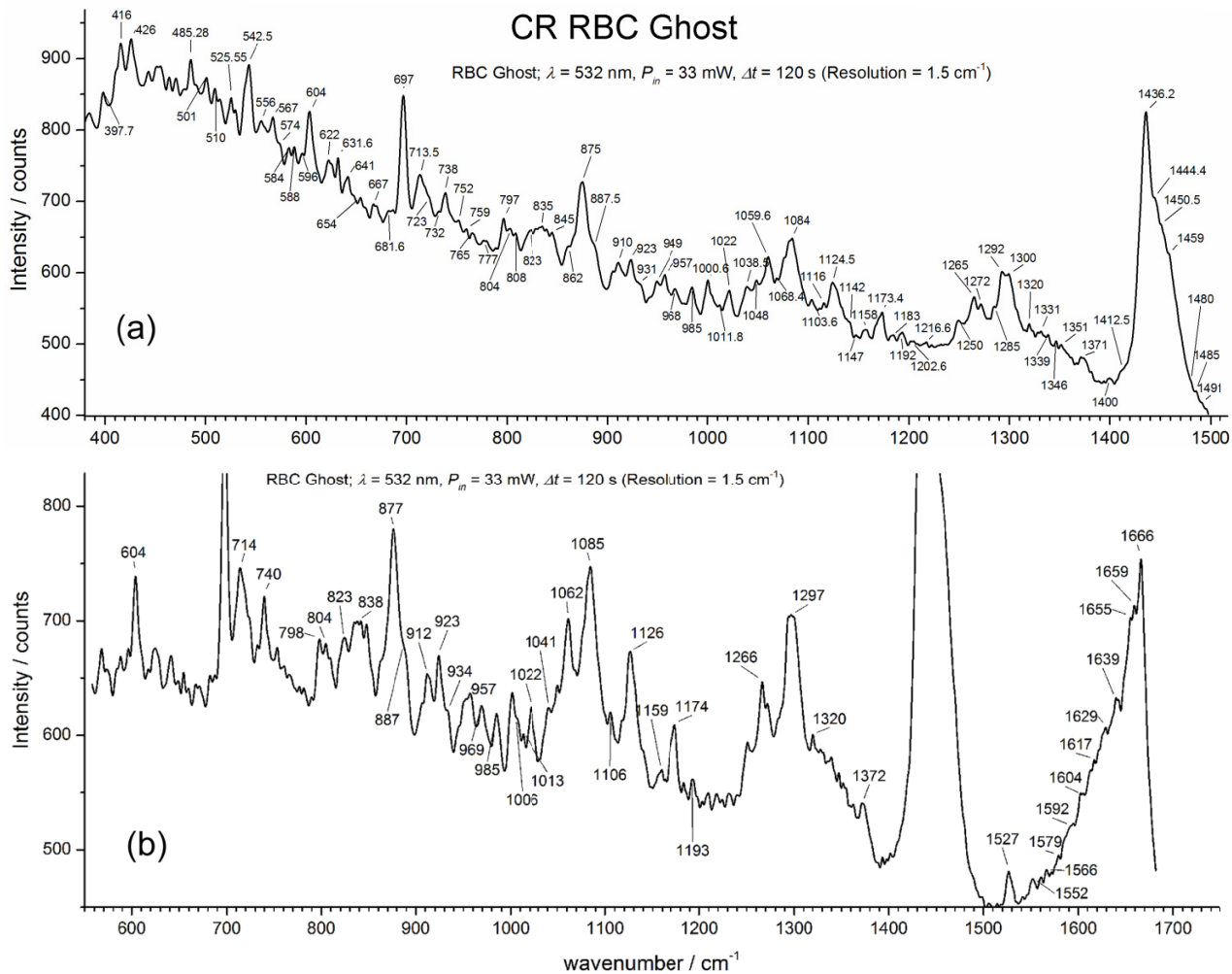
Figure S6. Raman spectra of RBC ghosts in PBS (1% w/v): two spectral ranges in (a) and (b) (exalted details in (b)). Spectral lines are typical of phospholipids/carbohydrates, amino acids and skeletal modes of carbohydrates. In the following Table on the left, main Raman assignment is reported.

Observed band position (cm^{-1})	Tentative assignment
542	S-S (P) [S27]
697	C-S (P) [S27]
877	Tyr ring (P) [S27]
934	Amide III (P) [S17]
957	Amide III (P) [S17]
1062	Skeletal mode (L) [S30]
1085	Skeletal mode (L) [S30]
1126	Skeletal mode (L) [S30]
1174	=C-C= (L) [S19]
1266	Amide III [S19]
1297	CH$_2$(L/P) [S19]
1432	CH$_2$ (L) [S30]
1527	C=C (carotenoids) [S31-S32]
1639	Amide I (P) [S17]
1655	Amide I (P) [S17]
1688	Amide I (P) [S30]

Erythrocyte ghosts were prepared following ref. [S10]. Average CR spectra (in two slightly shifted spectral ranges to cover all significant features) are shown in **Figure S6**. The observed spectral features reflect typical membrane constituents such as phospholipids, carbohydrates, proteins and carotenoids present in the plasma membrane [S11-S16], in good agreement with Raman spectra reported in refs. [S17-S19]. There is no significant contribution, as can be seen in the spectra, from residual membrane-bound Hb.

Surface-enhanced Raman Scattering Spectra (SERS) of live-RBC and RBC ghosts

Typical SERS spectra detected along the membrane scan are given in **Figures S7-S9**. They were acquired in different positions of the same cell, and showed spectral changes which denote sensitivity to the membrane environment explored in the scattering area. Here, we limit Raman assignment to highlighting clear membrane's contributions. We found an excellent agreement with the Raman spectra of ghost erythrocyte membranes reported by Mikkelsen et al. [S17] and Lippert et al. [S18]. In detail, by analysing the coincidence of recurrent peaks in correlation with the spontaneous Raman and SERS bands reported for membrane's molecular constituents [S20-S32] and the agreement with our experimental CR analysis of RBC ghosts (mainly membrane) reported in Fig. S6, we were able to identify significant membrane features into our SERS spectra of the viable cell. As for instance, our SERS spectra of the live RBC show strong evidences of carbohydrates-related vibrations, such as carbohydrates skeletal vibrations (400-700 cm^{-1}), C-O and C-C stretching (950-1200 cm^{-1}), as well as CH and CH$_2$OH related vibrations (1200-1500 cm^{-1}) [S20-S23]. Numerous bands were also assigned to amino acid markers of proteins, like aromatic residues Phenylalanine (Phe), Tyrosine (Tyr), and Tryptophan (Trp), besides protein conformation bands (Amide I: 1600-1680 cm^{-1}, Amide II: 1520-1600 cm^{-1}, Amide III: 1200-1300 cm^{-1}) [S24-S27] and bands assignable to the low-energy S-S (500-550 cm^{-1}) and C-S (600–670 cm^{-1}) vibrations in proteins [S28, S29]. Finally, extremely intense and well defined peaks showing very large signal to noise ratio were also matched with the phospholipid content: in particular, bands assignable to C-C skeletal vibration of lipids (1060 – 1130 cm^{-1}) and CH$_2$ deformation (1436 cm^{-1}) were frequently observed [S27, S30]. In particular strong lipid markers are visible in **Fig. S7(a)-(b),** but also in Fig. S8-S9. Other membrane's constituent bands, first observed by Lippert et al. [S18] and next ascribed to carotenoids [S31] (antioxidants of membrane lipid bilayer), were also present in both SERS spectra of live-RBC [Fig. S7(a)-(b)] and RBC ghost solution [Fig. S7(c)], *i.e.* the bands at 1156-1160 cm^{-1} and 1515-1527 cm^{-1} (see also ref. [S32] for assignment). As it can be seen in Fig. S7, the SERS spectrum of the RBC ghost solution (c) is found in good agreement with the SERS spectra of the viable cell (a)-(b).

Next **Figures S8-S9** show representative SERS spectra acquired along a raster scan (see inset of Fig. S8) of the viable cell. It is worth noticing that although spectra (6) and (7) in Fig. S9 include some spectral features ascribable to porphyrin (membrane-bound Hb) in the spectral range 1300-1640 cm^{-1} [S10], however these features appear accompanied by other spectral lines, such as 473, 727, 904, 1013, 1030, 1050, 1107, 1276, 1450, 1184-1188, 1314, 1355, 1438, 1652 cm^{-1}, which belong to membrane's lipids and proteins, also in agreement with ref. [S10].
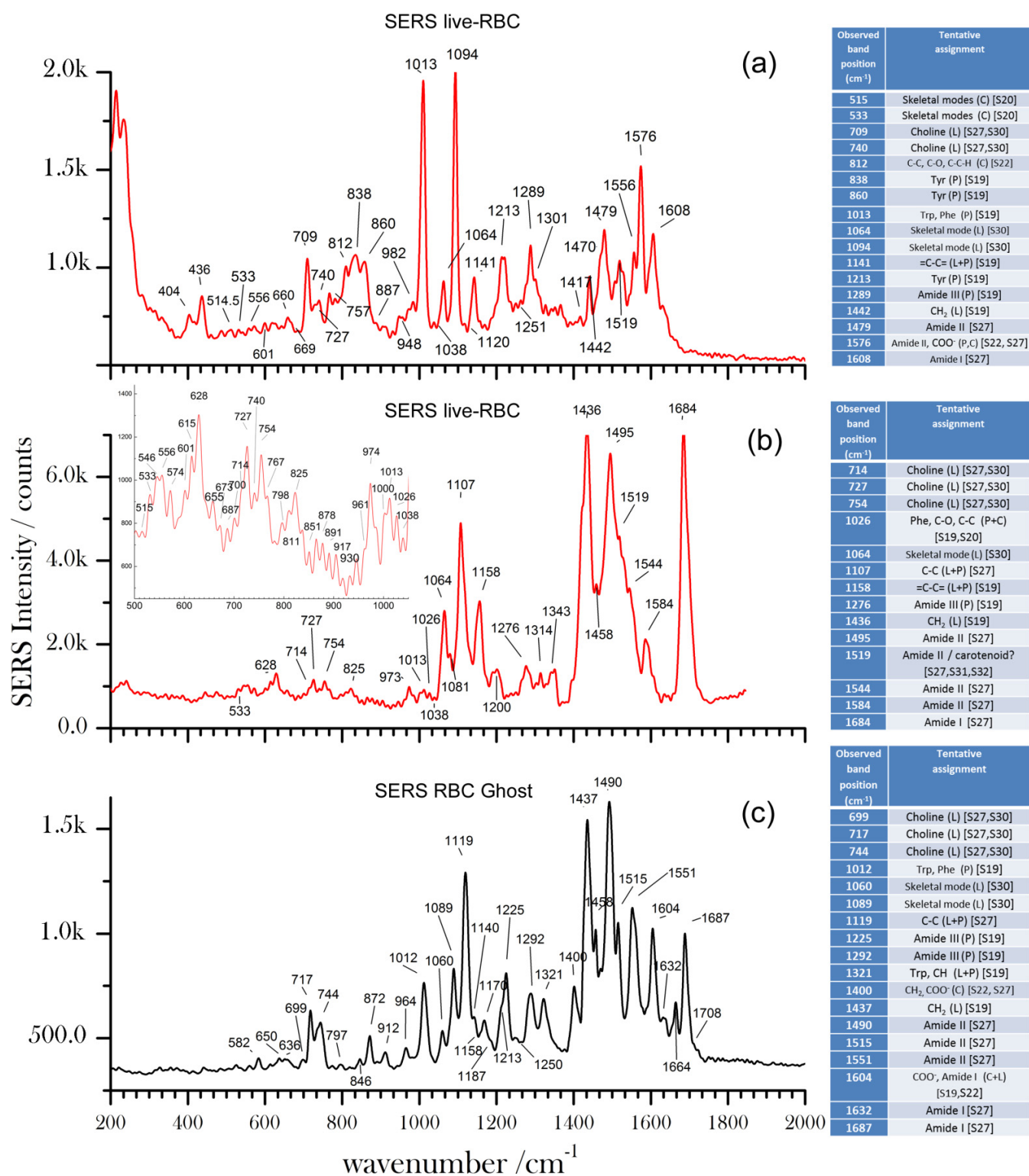
Figure S7. (a)-(b), SERS spectra acquired on live-RBC, in different positions at the border of the cell in contact with the SERS substrate. The spectra show strong evidence of lipid/carbohydrate markers, carotenoid and aromatic amino acids spectral features. (c), Average SERS spectrum of RBC ghost solution, here shown for comparison with (a)-(b): besides the excellent correspondence of the various plasma membrane markers, there is a very good agreement with the spectral features in the CR spectrum of RBC ghost solution (Fig. S6). The Tables on the right summarize the main spectroscopic assignment. Legend: P = Protein; L = Lipid; C = Carbohydrate. Incident power (532 nm) was P_{in}= 0.5 μW, and integration time Δt = 2 s.

Spectrum (1)

Observed band position (cm⁻¹)	Tentative assignment
427	Skeletal modes (C) [S20]
655	C-S (P) [S27]
812	C-C, C-O, C-C-H (C) [S22]
860	C-C-O (C) [S22]
904	Tyr (P) [S19]
1013	Tyr, Phe ring (P) [S19]
1128	Skeletal modes (L) [S30]
1217	Amide III (P) [S19]
1272	Amide III (P) [S19]
1314	CH₂(L) [S30]
1351	CH (L+P) [S19]
1405	-C-O- (C) [S27]
1462	CH₂ (L) [S19]
1544	-C=C- (L+P) [S19]
1596	Amide II (P) [S27]
1636	Amide I (P) [S19]
1676	Amide I (P) [S19]
1740	-C=O (L) [S27]

Spectrum (2)

Observed band position (cm⁻¹)	Tentative assignment
404	Skeletal modes (C) [S20, S21]
455	Skeletal modes (C) [S20, S21]
673	Amide IV
856	C-C-O (C) [S22]
921	C-C-H, C-C-O (C) [S22]
952	C-C-H and C-C-O (C) [S22]
1008	Trp, Phe ring (P) [S19]
1094	Skeletal modes (L) [S30]
1188	Amide III (P) [S19]
1205	Amide III (P)
1217	Tyr ring (P) [S19]
1276	Amide III (P) [S19]
1293	CH₂, CO(L+P) [S19,S22]
1446	CH₂ (L) [S19]
1523	C=C (carotenoids [S31, S32]
1596	Amide II (P) [S27]
1624	Amide I(P) [S19]
1672	Amide I (P) [S19]

Spectrum (3)

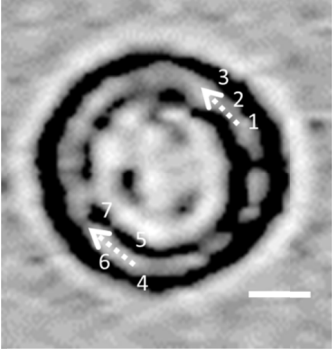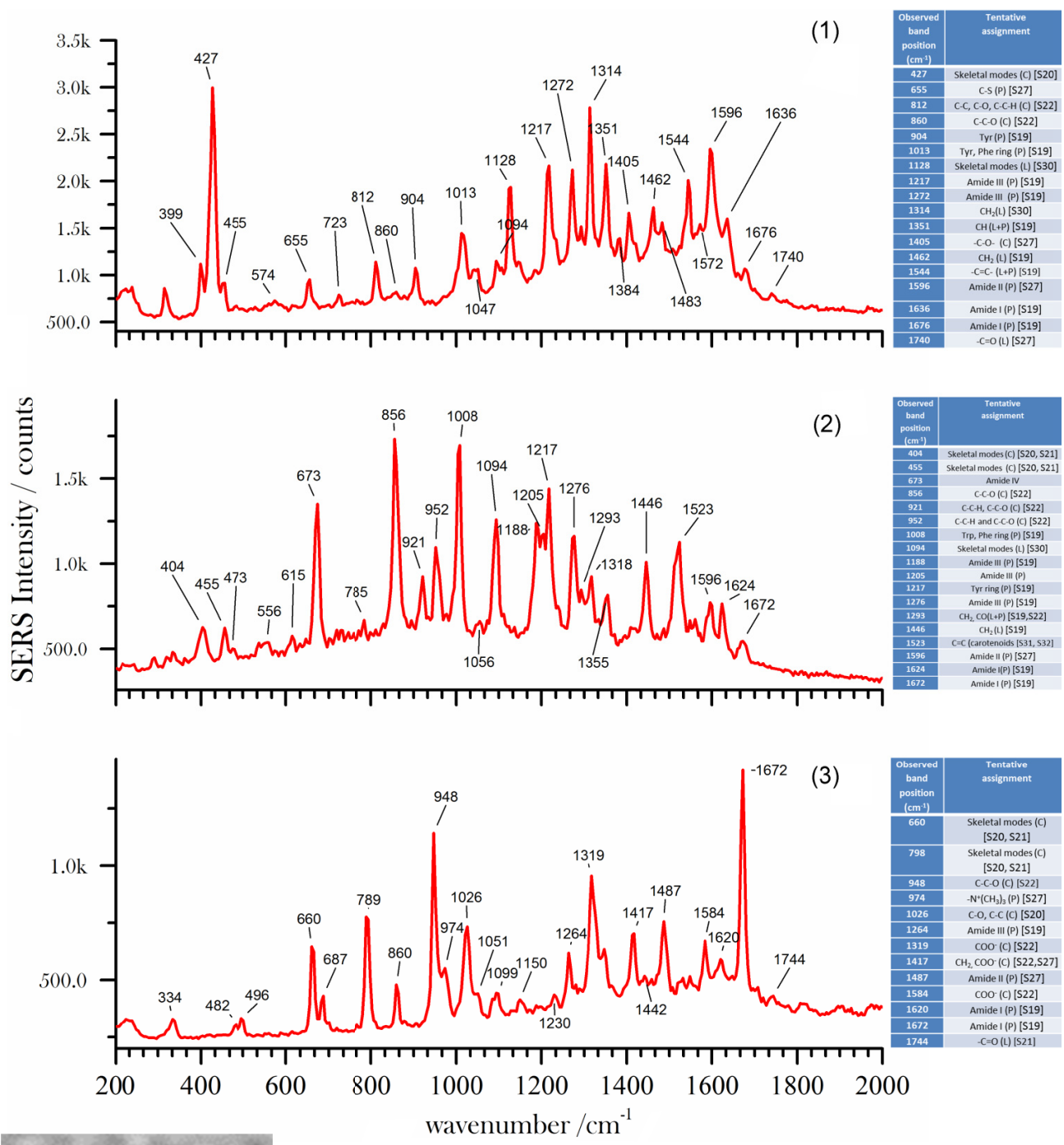| Observed band position (cm⁻¹)	Tentative assignment
660	Skeletal modes (C) [S20, S21]
798	Skeletal modes (C) [S20, S21]
948	C-C-O (C) [S22]
974	-N⁺(CH₃)₃ (P) [S27]
1026	C-O, C-C (C) [S20]
1264	Amide III (P) [S19]
1319	COO⁻ (C) [S22]
1417	CH₂, COO⁻ (C) [S22,S27]
1487	Amide II (P) [S27]
1584	COO⁻ (C) [S22]
1620	Amide I (P) [S19]
1672	Amide I (P) [S19]
1744	-C=O (L) [S21]

Figure S8. Representative SERS spectra acquired during a raster scan on a RBC, at the positions 1-3 (see inset on the left) with step of 400 nm along the viable RBC membrane: they denote sensitivity to the local membrane chemicals. SERS spectra in the remaining positions (4-7) are shown in Fig. S9. The Tables on the right of each spectrum summarize the major Raman assignment. Legend: P = Protein; L = Lipid; C = Carbohydrate. Incident power (532 nm) was P_{in} = 0.5 μW, and integration time Δt = 2 s. Scale bar in the optical image on the left is 4 μm. Represented positions of SERS acquisition are not in scale.
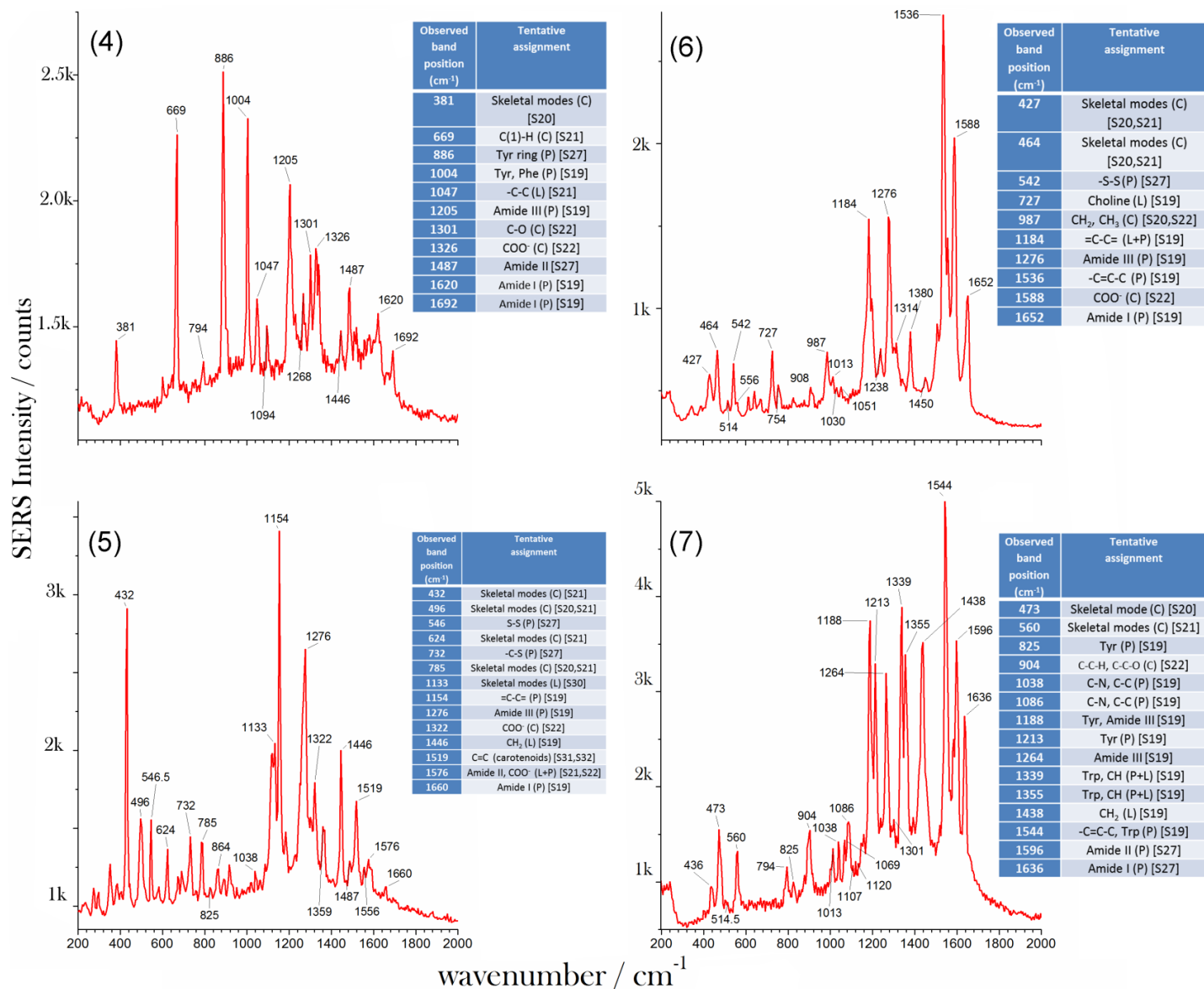
Figure S9. Representative SERS spectra from same line scan of Fig. S8, at positions (4)-(7), with step of 400 nm. The Tables on the right of each spectrum [(4)-(7)] summarize main Raman assignment. Legend: P = Protein; L = Lipid; C = Carbohydrate. Incident power (532 nm) was P_{in}= 0.5 μW, and integration time Δt = 2 s.

Supplementary References

S1.   Zachary, C. E., Jiao, Y. & Torquato, S. Hyperuniform Long-Range Correlations are a Signature of Disordered Jammed Hard-Particle Packings. *Physical Review Letters* 106, 178001 (2011).

S2.   Le Ru, E. C. & Etchegoin, P. G. Principles of Surface Enhanced Raman Spectroscopy and related plasmonic effects (Elsevier, Amsterdam, The Netherlands, 2009).

S3.   Cho, W. J., Kim, Y. & Kim, J. K. Ultrahigh-Density Array of Silver Nanoclusters for SERS Substrate with High Sensitivity and Excellent Reproducibility. *ACS Nano* **6**, 249-255 (2012).

S4.   Storkg, W. H. J., Lippitsa, J. M., & Mandel, M. Association of Crystal Violet in Aqueous Solutions. *The Journal of Physical Chemistry* 76, 1772-1775 (1972).

S5.   Han, Y. et al. Effect of Oxidation on Surface-Enhanced Raman Scattering Activity of Silver Nanoparticles: A Quantitative Correlation. *Analytical Chemistry* 83, 5873-5880 (2011).

S6.   Lee, P. & Meisel, D. Adsorption and surface-enhanced Raman of dyes on silver and gold sols. *The Journal of Physical Chemistry* **86**, 3391-3395 (1982).

S7.   Yan, B. et al. Engineered SERS substrates with multiscale signal enhancement: nanoparticle cluster arrays. *ACS Nano* **3**, 1190-1202 (2009).

S8.   Marzec KM et al. (2014) Red Blood Cells Polarize Green Laser Light Revealing Hemoglobin′s Enhanced Non-Fundamental Raman Modes. *Chem Phys Chem* DOI: 10.1002/cphc.201402598.

S9.   Wood, B. R. & McNaughton, D. Raman excitation wavelength investigation of single red blood cells in vivo. *J. Raman Spec.* 33, 517-523 (2002).

S10. Drescher D, Buechner T, McNaughton D, Kneipp J (2013) SERS reveals the specific interaction of silver and gold nanoparticles with hemoglobin and red blood cell components. *Phys Chem Chem Phys* 15:5364-5373.

S11. Gordon-Smith, T. Structure and function of red and white blood cells. *Medicine* 37, 119-124 (2009).

S12. Steck, T. The organization of proteins in the human red blood cell membrane A Review. *The Journal of cell biology* 62, 1-19 (1974).

S13. Fukuda, M., Fukuda, M. & Hakomori, S. Developmental change and genetic defect in the carbohydrate structure of band 3 glycoprotein of human erythrocyte membrane. *Journal of Biological Chemistry* 254, 3700-3703 (1979).

S14. Marchesi, V., Tillack, T. & Jackson, R. Chemical characterization and surface orientation of the major glycoprotein of the human erythrocyte membrane. *Proceedings of the National Academy of Sciences USA* 69, 1445-1449 (1972).

S15. Gahmberg, C. & Hakomori, S. External labeling of cell surface galactose and galactosamine in glycolipid and glycoprotein of human erythrocytes. *Journal of Biological Chemistry* 248, 4311-4317 (1973).

S16. Morrison, M. & Phillips. Exposed protein on the intact human erythrocyte. *Biochemistry* 10, 1766-1771 (1971).

S17. Mikkelsen, R. B., Verma, S. P. & Wallach, D. F. Effect of transmembrane ion gradients on Raman spectra of sealed, hemoglobin-free erythrocyte membrane vesicles. *Proceedings of the National Academy of Sciences USA* **75**, 5478-5482 (1978).

S18. Lippert, J. L., Gorczyca, L. E., Meiklejohn, G. A laser Raman spectroscopic investigation of phospholipid and protein configurations in hemoglobin-free erythrocyte ghosts. *Biochimica et Biophysica Acta - Biomembranes* **382**, 51–57 (1975).

S19. Wallach D.F., Verma S.P. Raman and resonance-Raman scattering by erythrocyte ghosts. *Biochim Biophys Acta.* **382** 542-551 (1975).

S20. Mrozek M.F., Weaver M.J. Detection and Identification of Aqueous Saccharides by Using Surface-Enhanced Raman Spectroscopy *Anal. Chem.* **74**, 4069-4075 *(*2002).

S21. She, C., Dinh, N. & Tu, A. Laser Raman scattering of glucosamine, N-acetylglucosamine and glucuronic acid. *Biochimica et Biophysica Acta* **372**, 345-357 (1974).

S22. Schmid T., Messmer A., Yeo B.S., Zhang, W.H., Zenobi, R. Towards chemical analysis of nanostructures in biofilms II: tip-enhanced Raman spectroscopy of alginates. *Anal. Bioanal. Chem.* **391**, 1907–1916 (2008).

S23. Feng, S. et al. Study on gastric cancer blood plasma based on surface-enhanced Raman spectroscopy combined with multivariate analysis. *Science China Life Sciences* **54**, 828-834 (2011).

S24. Zhu, G., Zhu, X., Fan, Q. & Wan, X. Raman spectra of amino acids and their aqueous solutions. *Spectrochimica Acta Part A: Molecular and Biomolecular Spectroscopy* **78**, 1187-1195 (2011).

S25. Overman, S. A. & Thomas, G. J. Raman Markers of Nonaromatic Side Chains in an α-Helix Assembly: Ala, Asp, Glu, Gly, Ile, Leu, Lys, Ser, and Val Residues of Phage Subunits. *Biochemistry* **38**, 4018-4027 (1999).

S26. Suh, J. & Moskovits, M. Surface-enhanced Raman spectroscopy of amino acids and nucleotide bases adsorbed on silver. *Journal of the American Chemical Society* **108**, 4711–4718 (1986).

S27. Schultz Z.D., Levin I.W. Vibrational spectroscopy of biomembranes. *Annu. Rev. Anal. Chem.* **4,** 343-366 (2011).

S28. Qian, W. & Krimm, S. Vibrational studies of the disulfide group in proteins. VI. General correlations of SS and CS stretch frequencies with disulfide bridge geometry. *Biopolymers* **32**, 1025-1033 (1992).

S29. Wart, H. & Scheraga, H. Agreement with the disulfide stretching frequency-conformation correlation of Sugeta, Go, and Miyazawa. *Proceedings of the National Academy of Sciences* USA **83**, 3064-3067 (1986).

S30. Gaber B.P., Yager P., Peticolas W.L. Interpretation of biomembrane structure by Raman difference spectroscopy. *Biophys. J.* **21,** 161-176 (1978).

S31. Lordi R. C. and Mendelsohn R. *Raman Spectroscopy of Membrane Constituents and Related Molecules,* in Membrane Spectroscopy, ed. Ernst Grell (Spreinger-Verlag, Berlin, 1981).

S32. Rusciano G., Pesce G., Salemme M., Selvaggi L., Vaccaro C., Sasso A., Carotenuto R. Raman spectroscopy of Xenopus laevis oocytes *Methods* **51,** 27–36 (2010).